

Rhombohedral distortion and percolation phenomena in B-site substituted perovskite ferroelectrics with enhanced piezoelectric response

Valeri Petkov^{1,*} and Vincenzo Buscaglia²

¹*Department of Physics, Central Michigan University, Mount Pleasant, Michigan 48859, USA*

²*Institute of Condensed Matter Chemistry and Technologies for Energy, National Research Council, via De Marini 6, 16149 Genoa, Italy*

 (Received 6 November 2020; revised 31 January 2021; accepted 6 April 2021; published 23 April 2021)

High-energy x-ray diffraction coupled with atomic pair distribution analysis and large-scale computer simulations are used to study the relationship between the local structure and piezoelectric response of an exemplary ferroelectric from the BaTiO₃ family where Ti is partially replaced by nonferroelectric Ce. Our results indicate that, likely, the increase in the piezoelectric response observed for Ce concentration <10% is due to an increased local rhombohedral distortion of the perovskite lattice. Despite a further increase in the distortion, the piezoelectric response for Ce concentration >10% decays quickly, likely because of rapidly increasing nonuniform strain fields due to the size mismatch between Ti- and Ce-centered octahedra and loss of electric dipoles due to the nonferroactivity of the latter. Thus, the transition between the observed two regimes of piezoelectric response does not appear to involve a crossing of a morphotropic phase boundary where the crystallographic symmetry changes abruptly but is likely to be percolative in nature. A similar behavior, referred to as tricritical phenomenon, is observed with other B-site substituted ferroelectrics from the BaTiO₃ family, indicating the presence of a common structural origin. Our results highlight the importance of chemical substitution-driven rhombohedral distortions in achieving control over the piezoelectric response of perovskite ferroelectrics, thereby providing a different perspective on the ongoing effort to improve their performance in practical applications.

DOI: [10.1103/PhysRevMaterials.5.044410](https://doi.org/10.1103/PhysRevMaterials.5.044410)

I. INTRODUCTION

Ferroelectrics based on BaTiO₃ are widely studied because of their excellent dielectric and electrocaloric properties [1–5]. The parent BaTiO₃ compound has a perovskite-type structure with a general formula ABO₃, where B-type ions (Ti⁴⁺) are sixfold coordinated by oxygen ions (O²⁻) forming a network of corner-sharing octahedra, and A-type ions (Ba²⁺) occupy the open space between the octahedra. The appearance of spontaneous polarization in BaTiO₃ is related to a displacement of Ti atoms from the geometrical center of the oxygen octahedra. At high temperature, BaTiO₃ exhibits a centrosymmetric cubic structure (space group *Pm-3m*) and no spontaneous polarization. Upon cooling, it undergoes a sequence of first-order phase transitions from the paraelectric cubic phase to ferroelectric phases with tetragonal (space group *P4mm*), orthorhombic (space group *Amm2*), and rhombohedral (space group *R3m*) crystallographic symmetry. The transitions take place at 398, 278, and 183 K, respectively. The net polarization in the noncentrosymmetric ferroelectric phases appears directed parallel to the edge of the unit cell of the aristotype cubic perovskite lattice (i.e., $\langle 001 \rangle_c$ direction), along a face diagonal (i.e., $\langle 011 \rangle_c$ direction) and a body diagonal (i.e., $\langle 111 \rangle_c$ direction) of that cell, respectively [6–9]. In the so-called order-disorder model of the phase transitions, Ti atoms in BaTiO₃ are assumed to be always displaced along the cube diagonals. That is, at high temperature, all eight

equivalent $\langle 111 \rangle_c$ directions are allowed, and at low temperature, the displacements all adopt either the same orientation, leading to an average rhombohedral symmetry, or two or three preferred directions, leading to an average tetragonal or orthorhombic symmetry, respectively [10–12]. On the other hand, the so-called displacive model of the phase transitions assumes that the equilibrium position of each Ti atom is in the middle of the oxygen octahedra for the high-temperature cubic phase, but appears displaced microscopically in the $\langle 111 \rangle_c$, $\langle 011 \rangle_c$, or $\langle 001 \rangle_c$ macroscopic polarization directions for the rhombohedral, orthorhombic, and tetragonal ferroelectric phases, respectively [13,14]. Recent studies indicate that the transitions between the ferroelectric phases of BaTiO₃ indeed exhibit a mix of order-disorder and displacive characters [15–22]. The transitions are accompanied by a strong dielectric softening, as indicated by the presence of distinct maxima in the permittivity, and anomalies in the thermal, mechanical, and piezoelectric properties, offering promise for device applications. However, owing to the strong temperature dependence of its dielectric properties, specifically the abrupt change of the piezoelectric response near the transitions between its ferroelectric phases, BaTiO₃ is hardly used in pure form. Chemical substitution at either the Ba or Ti site, or both, is widely used to prepare ferroelectric solid solutions with an increased and temperature-stable piezoelectric response that have proven very useful in applications ranging from sensors and actuators to optical and memory devices [4,5].

In addition to increasing the piezoelectric response, chemical substitution involving aliovalent ions such as, for example, Bi³⁺ at the A-site and Nb⁵⁺ at the B-site, often leads to the

*petko1vg@cmich.edu

formation of complex defect dipoles and oxygen vacancies that locally modify the electrostatic fields and change the transition temperatures [23–25]. Likewise, chemical substitution involving isovalent ions such as, for example, Sr^{2+} at the A-site and Zr^{4+} at the B-site, can both modify the piezoelectric response and induce local strain inhomogeneities, leading to changes in the transition temperatures [26–28]. Despite years of investigation, however, the exact role of the chemical substitution in determining the piezoelectric response and temperature of ferroelectric transitions in BaTiO_3 -based ferroelectrics is still unclear. Frequently evoked models attribute it to the existence of a morphotropic boundary separating polar phases with different crystallographic symmetry, low-symmetry bridging phases facilitating polarization rotation, random electric fields, and thermodynamic criticality [29–41]. The reason is the structural complexity of the resulting solid solutions and related complex physical phenomena affecting their ferroelectric behavior. Identifying the phenomena and understanding their individual contribution to the observed piezoelectric response is a prerequisite to taking control over the useful properties of BaTiO_3 -based ferroelectrics. Here, we concentrate on solid solutions where the increased piezoelectric response and changes in the transition temperatures are largely due to the significant difference between the size of Ti^{4+} and the isovalent ion that replaces it at the B-site of the perovskite lattice. In particular, we study $\text{BaTi}_{1-x}\text{Ce}_x\text{O}_3$ ferroelectrics where Ti^{4+} ions (radius $r = 0.605 \text{ \AA}$ for octahedral coordination) are partially replaced by nonferroactive Ce^{4+} ions (radius $r = 0.87 \text{ \AA}$ for octahedral coordination). Initial studies showed a highly nonlinear variation of the piezoelectric response and ferroelectric transition temperatures with Ce content, including the presence of a broad maximum in the former at a Ce concentration of $\sim 10\%$. The studies also confirmed the expected presence of distinct Ti- and Ce-centered octahedra in the solid solutions and suggested them as a possible structural origin of the observed unusual piezoelectric response [42,43]. The precise relationship between the former and the latter, however, has remained unclear, prompting the need for a further investigation. Using advanced x-ray scattering techniques and three-dimensional (3D) structure modeling geared toward revealing both the average and local crystal structure in good detail, we find that the enhanced piezoelectric response observed [42] at a relatively low Ce^{4+} concentration ($0.1 \leq x$) is due to an increased local rhombohedrality, i.e., increased Ti off centering, and reduced polarization anisotropy. Despite the further increased and not-decreased Ti off centering as suggested by earlier studies [43], the piezoelectric response of $\text{BaTi}_{1-x}\text{Ce}_x\text{O}_3$ solid solutions with higher Ce content, including Curie temperature, diminish due to a frustration of the cooperative ferroelectric order. Thus, the transition between these distinct regimes of ferroelectric behavior does not appear to involve breaking of the crystallographic symmetry but is likely to be percolative in character. It is due to geometric criticality related to the fast growth of nonuniform strain fields near corner-sharing Ti-O_6 and Ce-O_6 octahedra and concurrent loss of electric dipoles that increasingly weaken the long-range ferroelectric order in the perovskite lattice. Our findings are a step toward a better understanding of the piezoelectric response of BaTiO_3 -based ferroelectrics and are likely to be relevant to many other

B-site substituted ferroelectric oxides from the perovskite family.

II. EXPERIMENT

A. Sample preparation

Substituted $\text{BaCe}_x\text{Ti}_{1-x}\text{O}_3$ ferroelectrics with $x = 0, 0.05, 0.10, 0.15, 0.20,$ and 0.30 were prepared by a classical solid-state route using electronic grade nanocrystalline raw materials. Stoichiometric amounts of TiO_2 (Toho Titanium, Chigasaki, Japan), CeO_2 (VP AdNano[®] Ceria 50, Evonik Degussa, Germany), and BaCO_3 (Solvay Bario e Derivati, Massa, Italy) powders were wet mixed in aqueous suspension for 24 h using polyethylene jars and zirconia media. After freeze drying, the mixtures were calcined in air for 4 h at 1273 K. The final powders, after sieving, were isostatically pressed at 100 MPa forming cylindrical bodies with a diameter of ~ 1 cm. The bodies were sintered for 4 h in air at either 1723 ($x = 0, 0.05$ and $x = 0.10$) or 1823 K ($x = 0.15-0.30$). Phase purity was verified by in-house x-ray diffraction (XRD) [42,43]. The sintered bodies were grinded to fine powders and subjected to high-energy synchrotron XRD experiments described below.

B. Synchrotron XRD measurements and crystal structure constrained fits to the diffraction data

High-energy XRD patterns for the ferroelectrics were collected at the beamline 11-ID-B at the Advanced Photon Source at the Argonne National Laboratory using x rays with energy of 86.7 keV ($\lambda = 0.143 \text{ \AA}$). The instrument was calibrated using Si powder (NIST) standard. Each sample was sealed in a glass capillary and measured in transmission mode. An empty glass capillary was measured separately. Scattered intensities were collected with a two-dimensional (2D) amorphous Si detector. Two sets of XRD patterns were collected for each sample. One of the patterns was collected with the detector positioned 1000 mm away from the sample to achieve high- q resolution necessary for successful Rietveld analysis [44], where the wave vector q is defined as $q = 4\sin(\theta)/\lambda$, and θ is the Bragg angle. Experimental patterns for $\text{BaCe}_x\text{Ti}_{1-x}\text{O}_3$ ferroelectrics are shown in Fig. 1.

Diffraction patterns collected in this way, however, extend to q values of $\sim 12 \text{ \AA}^{-1}$ only, which renders them unsuitable for analysis in real space in terms of atomic pair distribution functions (PDFs) [45,46]. Therefore, another set of diffraction patterns was collected with the detector positioned 300 mm away from the sample. Diffraction patterns collected in this way suffer poor q -space resolution and are not suitable for Rietveld analysis. However, they extend to q values as high as 30 \AA^{-1} , rendering them very suitable for atomic PDF analysis that has proven very useful in structure studies of crystalline materials with intrinsic disorder, including perovskite ferroelectrics [43,47–52]. The atomic PDFs were derived from the patterns as follows: at first, the separately measured signal arising from the glass capillary and sample environment, largely including air scattering, was subtracted from the respective high-energy XRD patterns. Then corrections for absorption in the sample and inelastic (Compton scattering) were applied following long-established procedures using an

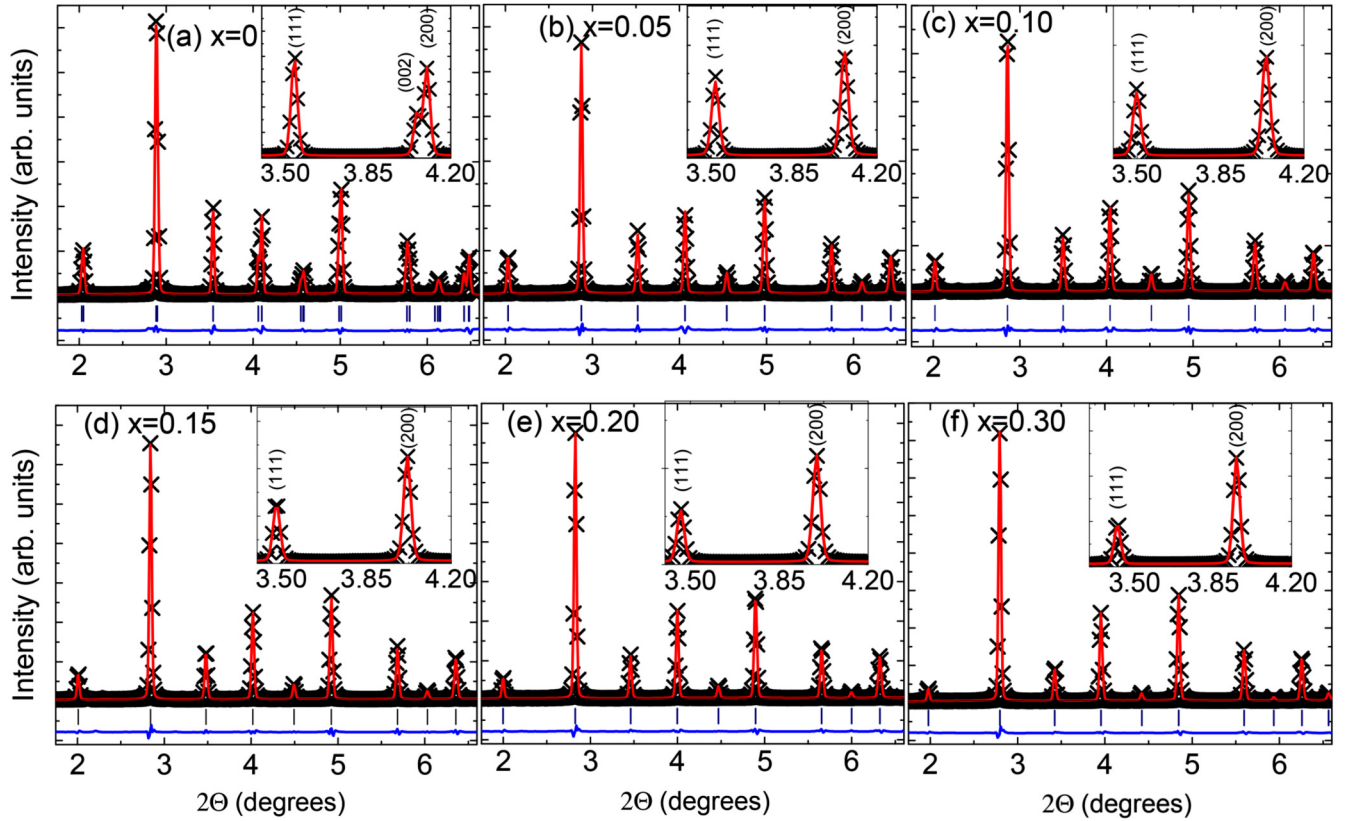


FIG. 1. Experimental (symbols) and Rietveld fit (red line) x-ray diffraction (XRD) patterns for $\text{BaTi}_{1-x}\text{Ce}_x\text{O}_3$ ferroelectrics. For clarity, the residual difference (blue line) is shifted by subtracting a constant. The diffraction feature at about 4° in the XRD patterns for BaTiO_3 (see the inset) appears split. Its two components can be indexed as (002) and (200) Bragg peaks in a tetragonal lattice (space group $P4mm$). That feature appears as a singlet in the XRD patterns for the solid solutions and can be indexed as a (200) Bragg peak in a cubic lattice. The feature at about 3.5° can be indexed as a (111) peak in the same cubic lattice (space group $Pm-3m$). Accordingly, the XRD pattern for BaTiO_3 is Rietveld fit with a tetragonal and those for the solid solutions with a cubic model. The XRD patterns for the solid solutions can also be reasonably well fit with an orthorhombic (space group $Amm2$) and rhombohedral (space group $R3m$) structure models [see Fig. 4(c)]. Unit cell volumes for the crystal lattices Rietveld fit against the experimental XRD patterns are summarized in Fig. 4(a).

improved version of the software RAD [46]. The resulting data were scaled into absolute units and converted to the so-called reduced structure factors $q[S(q)-1]$. Finally, using a Fourier transformation, the reduced structure factors were converted to the respective atomic PDFs $G(r)$. As an example, the reduced structure factor and $G(r)$ for $\text{BaCe}_{0.3}\text{Ti}_{0.7}\text{O}_3$ are shown in Fig. 2. Atomic PDFs for all $\text{BaCe}_x\text{Ti}_{1-x}\text{O}_3$ ferroelectrics studied here are shown in Fig. 3.

Note that, by definition, $G(r) = 4\pi r[\rho(r) - \rho_0]$, where $\rho(r)$ is the local and ρ_0 is the average atomic number density, respectively. In this respect, the atomic PDF resembles the so-called Patterson function that is widely used in traditional crystallography. However, while the Patterson function peaks at interatomic distances within the unit cell of a crystal, the atomic PDF peaks at all distinct interatomic distances occurring in a material, be it perfectly crystalline or not. Furthermore, while both Rietveld analysis of powder XRD patterns and single crystal structure analysis in terms of Patterson functions concentrate on sharp Bragg peaks in XRD data, atomic PDFs consider both the Bragg peaks and the diffuse-type scattering components of XRD data. In this way, both the perfect atomic order, manifested in the former, and all local structural “distortions,” manifested in the latter, are reflected

in the experimental PDFs. In this respect, atomic PDF analysis goes beyond traditional techniques for determining the atomic structure of crystals that typically reveal well their long-range periodic features, i.e., average structure, alone [45].

III. DIFFRACTION DATA ANALYSIS AND 3D STRUCTURE MODELING

To ascertain the average crystal structure of studied solid solutions, we carried out Rietveld analysis of the high- q resolution XRD patterns. The analysis was performed using the software GSAS II [44]. The diffraction pattern for each sample was fit with structure models based on the cubic, tetragonal, orthorhombic, and rhombohedral phases known to occur with ferroelectrics from the BaTiO_3 family. Exemplary results of the Rietveld fits are shown in Fig. 1. Goodness-of-fit indicators R_w for all fits are summarized in Fig. 4. Data for the volume of the unit cell of the refined crystal lattices and values for the rhombohedral angle derived from Rietveld fits based on the rhombohedral model are also summarized in Fig. 4.

In line with the finding of earlier studies [42], Rietveld analysis performed here shows that, at room temperature, the average crystal structure of BaTiO_3 appears to be tetragonal.

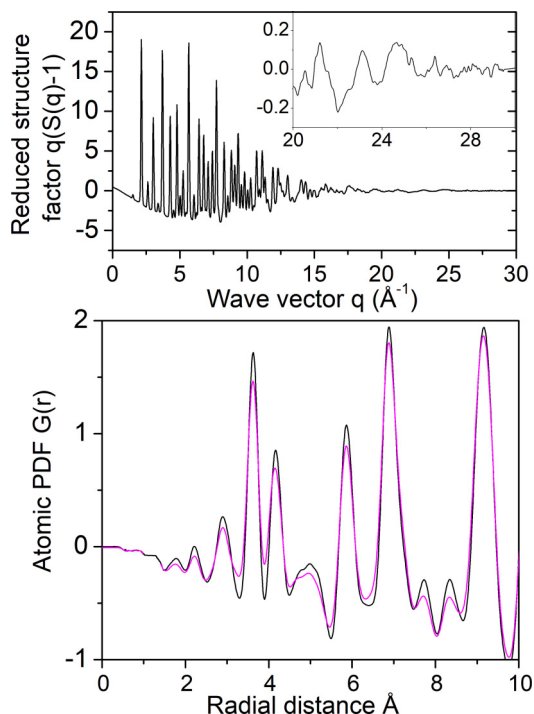


FIG. 2. (upper panel) Experimental structure function for $\text{BaTi}_{0.7}\text{Ce}_{0.3}\text{O}_3$. Physical oscillations are present to the maximum wave vector of 30 \AA^{-1} reached in the present synchrotron x-ray diffraction (XRD) study (see the insert). (lower panel) Atomic pair distribution functions (PDFs) obtained by a Fourier transformation of the whole range of experimental structure function data extending to 30 \AA^{-1} (black line) and a reduced range of the experimental structure function data extending to 20 \AA^{-1} only (magenta line). As it may be expected, the low- r peaks of the latter, those just below and above 2 \AA , appear less sharp in comparison to the low- r peaks in the former. The peaks, however, do not change their position and shape significantly, indicating that they are not Fourier transformation termination ripples and/or due to systematic errors that tend to pile up at high q values [45] but truly reflect the near neighbor metal-oxygen distances in $\text{BaTi}_{0.7}\text{Ce}_{0.3}\text{O}_3$.

Also, in line with the findings of earlier studies [43], the XRD patterns for the solid solutions appear almost equally well fit with models based on the four crystal phases of BaTiO_3 [see the R_w values in Fig. 4(c)]. For convenience, the average crystal structure of such solid solutions is often described in terms of a pseudocubic lattice symmetry [53–55]. Here, we adopt this description, as done in earlier studies [42,43]. Notably, the volume of the unit cell of the model crystal lattices is seen to increase uniformly with Ce content [see Fig. 4(a)]. The result indicates that Ce atoms are incorporated in the B-site of the perovskite lattice as Ce^{4+} ions, and not in the A-site of the lattice as Ce^{3+} ions (radius $r = 1.31 \text{ \AA}$ for 12-fold coordination) [42,43,47]. If the latter were true, the volume would have decreased with the Ce content because Ce^{3+} is smaller than Ba^{2+} (radius $r = 1.61 \text{ \AA}$ for 12-fold coordination) in size. Interestingly, the rhombohedral angle of the Rietveld refined structure models with an average rhombohedral symmetry is seen to increasingly deviate from the value of 90° with Ce content [see Fig. 4(b)], indicating an increased rhombohedral distortion of the perovskite lattice.

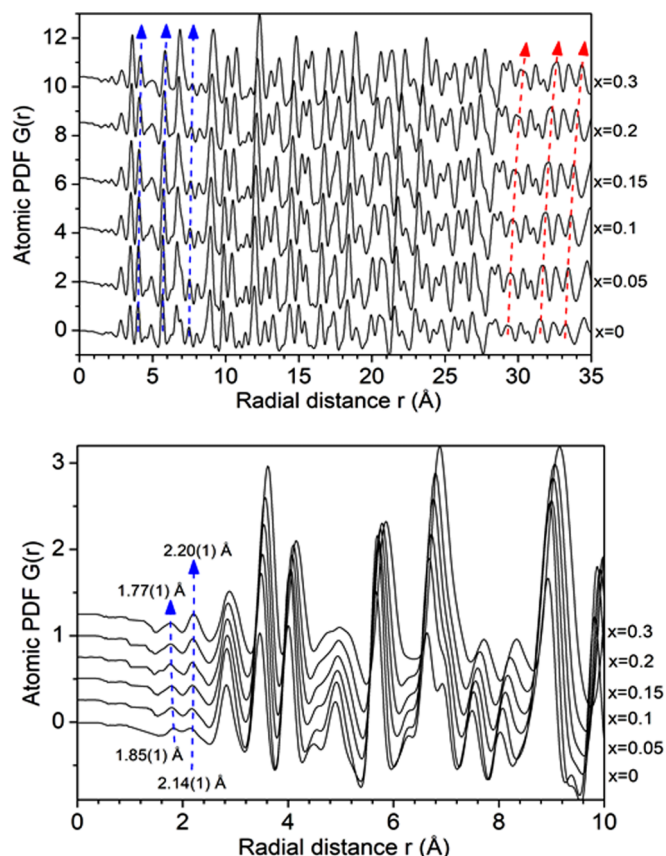


FIG. 3. (upper panel) Experimental total atomic pair distribution functions (PDFs) for $\text{BaTi}_{1-x}\text{Ce}_x\text{O}_3$ ferroelectrics ($x = 0, 0.05, 0.1, 0.15, 0.20,$ and 0.3). Arrows emphasize the different evolution of the local (blue arrows) and average (red arrow) crystal structure with Ce content x . In particular, the former undergoes a subtle evolution with x , whereas the latter evolves markedly. Note that the marked shift of the longer range atomic pair distances (red arrows) is consistent with the linear increase in the volume of the pseudocubic unit cell derived by Rietveld analysis [compare with data in Fig. 4(a)], both reflecting the evolution of the average crystal structure of the solid solutions with x . (second row) Low- r region of the experimental PDFs highlighting the evolution of the first two physical peaks (blue arrows) with Ce content. The peaks reflect ME -oxygen bonding distances, where $ME = \text{Ti}$ and Ce . In particular, they reflect the presence of three short [$1.85(1) \text{ \AA}$] and three long [$2.14(1) \text{ \AA}$] Ti-oxygen bonds in BaTiO_3 . The position of the first and second peak gradually shifts, respectively, to lower [$1.77(1) \text{ \AA}$] and higher- r [$2.20(1) \text{ \AA}$] values with Ce content, reflecting the evolution of ME -O bonding distances. The peaks have similar intensity with BaTiO_3 ($x = 0$), and the intensity of the second peak increases in comparison with that of the first one with Ce content. As discussed in the text, the increase is due to the appearance of Ce-oxygen bonds in the solid solutions whose length is like that of the longer Ti-oxygen bonds. Note that each arrow in the upper and lower panel is unique in the sense that it connects the maxima of corresponding peaks in the PDF data.

The increase is, however, puzzling because, contrary to the case of BaTiO_3 , the characteristic features in the experimental XRD patterns at 3.5° and 4° (see Fig. 1) appear as singlets for the solid solutions, indicating an increase and not a decrease in the average crystal symmetry with Ce content. The

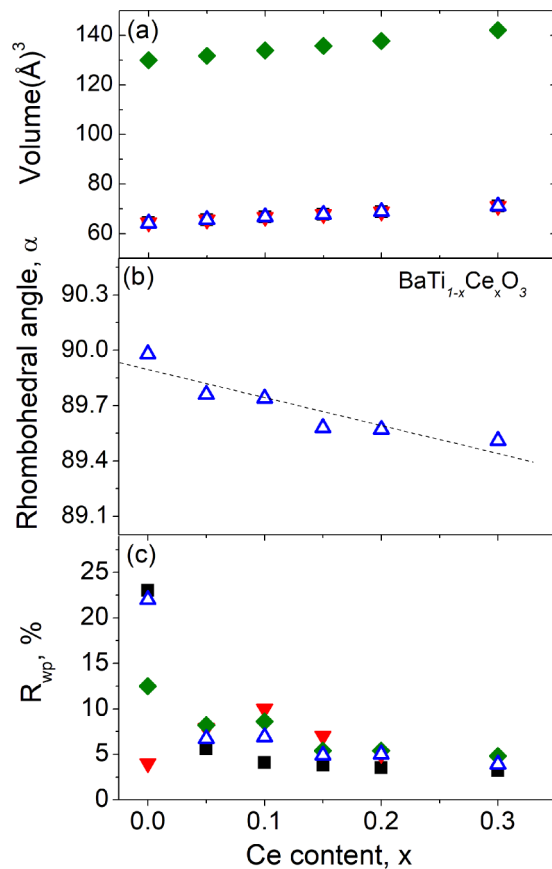


FIG. 4. (a) Evolution of the unit cell volume in $\text{BaTi}_{1-x}\text{Ce}_x\text{O}_3$ ferroelectrics with Ce content, as obtained by Rietveld fits to their high-energy x-ray diffraction (XRD) patterns. (b) Evolution of the rhombohedral angle for the fits featuring a rhombohedral crystal symmetry. The broken line is a guide to the eye. The angle diminishes with x , indicating an increase in the rhombohedral distortion of the perovskite lattice with Ce content. (c) Evolution of the goodness-of-fit factor for Rietveld fits to high-energy XRD patterns for $\text{BaTi}_{1-x}\text{Ce}_x\text{O}_3$. The factors correspond to fits based on crystal lattices with a cubic (black squares), tetragonal (red triangles), orthorhombic (green rhombuses), and rhombohedral (blue triangles) crystal symmetry. Data both in (a) and (b) are seen to evolve linearly with Ce content, indicating that the solid solutions are single phase. Data in (c) show that the average crystal structure of BaTiO_3 studied here appears to be tetragonal (lowest R_w factor). The crystal structure of the solid solutions is almost equally well described by the tested four structure models. Therefore, and in line with results of prior studies [42,43], that structure is considered to have a pseudocubic symmetry.

ambiguous outcome of Rietveld analysis can be attributed to the limited ability of sharp Bragg peak-based crystallography to clearly reveal likely local structural distortions in chemically substituted BaTiO_3 . Atomic PDF analysis conducted below has proven more useful in this respect [27,43,48–52].

Next, we inspected the experimental PDFs for signatures of local structural distortions in the solid solutions, known to occur with the members BaTiO_3 and BaCeO_3 , both of which are built of corner-sharing ME -oxygen octahedra ($ME = \text{Ti}, \text{Ce}$). It is well established [6–10] that the octahedra in the former are not tilted with respect to each other, but Ti atoms

are off centered, rendering the material ferroelectric already at room temperature. The displacement of Ti and O atoms from their symmetry sites in the aristotype cubic phase results in changes in Ti-O bond lengths. In the case of a tetragonal lattice distortion, there appear to be one long, one short, and 4 “normal” Ti-O bonds with a length ($r_{\text{Ti-O}} = 2.005 \text{ \AA}$) close to the sum of the ionic radii of oxygen and Ti for octahedral coordination. In the case of an orthorhombic lattice distortion, this becomes two long, two short, and two normal Ti-O bonds, while for the rhombohedral lattice distortion, there are three short and three long Ti-O bonds [7,8], as illustrated in Fig. 5. On the other hand, the octahedra in the latter are tilted, but Ce atoms are hardly off centered, rendering the material non-ferroelectric. Accordingly, all Ce-O bonding distances appear virtually the same [$r_{\text{Ce-O}} = 2.24(1) \text{ \AA}$] [56–59], as also illustrated in Fig. 5. The inspection revealed that near neighbor ME -oxygen bonding distances in all studied samples appear as two distinct, low- r PDF peaks (see Fig. 3). A test for PDF data quality verified that the peaks are physical in nature and not an experimental artifact, as shown in Fig. 2. They are seen to appear at 1.85(1) and 2.14(1) \AA for pure BaTiO_3 and evolve, respectively, to 1.77(1) and 2.20(1) \AA for $\text{BaTi}_{0.7}\text{Ce}_{0.3}\text{O}_3$. The presence of two distinct ME -oxygen bonding distances in $\text{BaTi}_{1-x}\text{Ce}_x\text{O}_3$ ferroelectrics, including pure BaTiO_3 , indicates that their local atomic structure is largely of a rhombohedral type at room temperature. Evidently, while the average crystal structure appears tetragonal in BaTiO_3 and pseudocubic in the solid solutions, as determined by Rietveld analysis of XRD patterns, largely, the local symmetry of the crystal lattice in $\text{BaTi}_{1-x}\text{Ce}_x\text{O}_3$ ferroelectric appears reduced to rhombohedral for $0 \leq x \leq 0.3$, as revealed by experimental PDFs.

Having established the presence of a distinct local and average crystal structure in the studied ferroelectrics, we looked for structure models that incorporate both in a consistent manner. For the purpose, initially, we fit the experimental atomic PDFs with models constrained to the four structure types exhibited by BaTiO_3 , taking advantage of the fact that, when considered over an extended range of real-space distances, the PDFs are indeed sensitive to both the local and average crystal structure (see Fig. 1). Fit results for pure BaTiO_3 are shown in Figs. 6(a)–6(d). In line with the findings of Rietveld analysis, the higher- r part of the PDF for BaTiO_3 is reproduced well by a structure model based on a tetragonal perovskite lattice. However, this model fails to reproduce well the equal intensity of the first and second PDF peaks, i.e., the presence of three short and three long Ti-O distances in the studied BaTiO_3 [see the inset in Fig. 6(b)]. The intensity ratio is reproduced well by a model based on a rhombohedral perovskite lattice [see the inset in Fig. 6(d)], which also reproduces reasonably well the higher- r part of the PDF data. The result showed that a structure model featuring a perovskite lattice built of rhombohedrally distorted ME -oxygen octahedra is a realistic description of BaTiO_3 . Similar results were obtained for the solid solutions, except that even the rhombohedral model could not reproduce well the relative increase in the intensity of the second PDF peak [2.20(1) \AA] with respect to that of the first one [1.77(1) \AA] with Ce content (see Fig. 7). The result showed that a model featuring a perovskite lattice built of rhombohedrally distorted ME -oxygen octahedra alone would be merely a plausible approximation to their atomic-level structure.

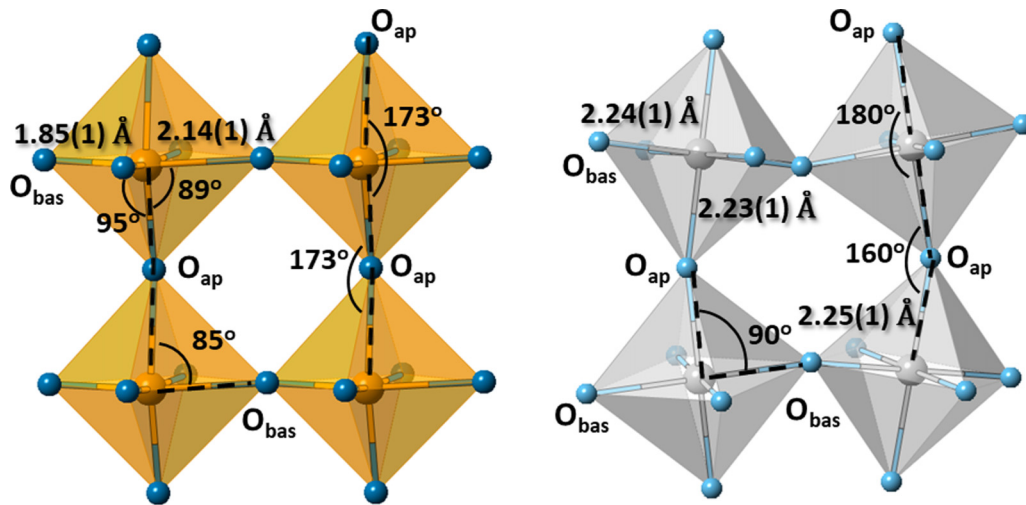


FIG. 5. (left) Fragment from the atomic structure of the rhombohedral (space group $R3m$) polymorph of BaTiO_3 [7]. (right) Fragment from the atomic structure of the room-temperature orthorhombic (space group $Pbnm$) polymorph of BaCeO_3 [56–59]. Both structures feature a perovskite-type lattice of $ME\text{-O}_6$ octahedra ($ME = \text{Ti}$ and Ce), where Ba atoms (not shown) occupy 12-fold-coordinated cavities between the octahedra. Ti atoms in rhombohedral BaTiO_3 are displaced from the geometrical center of the oxygen octahedra along $\langle 111 \rangle_c$ direction (cube diagonal) of the aristotype cubic BaTiO_3 . As a result, it exhibits three short [1.85(1) Å] and three long [2.14(1) Å] Ti-O distances. Due to Ti off centering, oxygen-Ti-oxygen angles involving at least one basal oxygen atom O_{bas} appear at 85°, 89°, and 105°. Ti-O₆ octahedra are not tilted with respect to each other, and Ti-O_{ap}-Ti and O_{ap}-Ti-O_{ap} angles involving apical oxygen atoms O_{ap} appear at 173°. The small deviation from 180° is due to Ti off centering. Ce atoms in BaCeO_3 are virtually not displaced from the center of oxygen octahedra. Accordingly, all Ce-O distances are nearly the same [2.24(1) Å]. Also, all oxygen-Ce-oxygen bond angles involving at least one O_{bas} atom are the same and equal to 90°. The oxygen octahedra are, however, tilted with respect to each other, rendering Ce-O_{ap}-Ce angles as small as 160°. Ti, Ce, and oxygen atoms are shown as brown, gray, and blue balls, respectively.

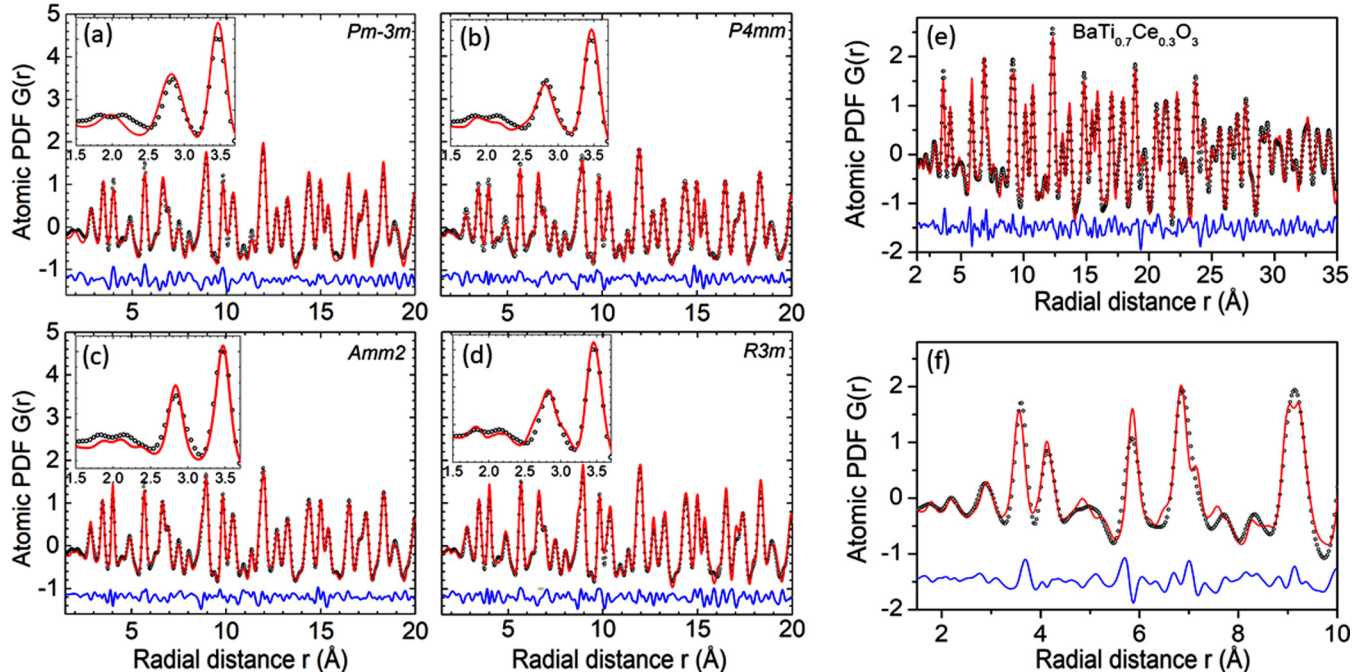


FIG. 6. (a)–(d) Experimental (symbols) and model fit (red line) atomic pair distribution functions (PDFs) for BaTiO_3 . The type of the model is shown for each of the fits. The low- r part of the PDFs is shown in the insets. For clarity, the residual difference (blue line) is shifted by subtracting a constant. The rhombohedral (space group $R3m$) model reproduces the nearest neighbor Ti-O distances, seen as equal in magnitude peaks positioned at 1.85(1) and 2.14(1) Å, best in comparison with the other models. (e) Experimental (symbols) and model computed (red line) PDF for $\text{BaTi}_{0.7}\text{Ce}_{0.3}\text{O}_3$ ferroelectric. (f) Low- r part of the data shown in (e). The model features a phase mixture of 0.7 mol rhombohedral BaTiO_3 , where Ti-O octahedra are distorted, and 0.3 mol orthorhombic BaCeO_3 , where Ce-O octahedra are not distorted. It is consistent with the low- r experimental data and reproduces the first two PDF peaks at 1.77(1) and 2.20(1) Å, including their different intensity. The model, however, does not reproduce well fine PDF features at longer- r distances [e.g., see the PDF peaks at 5 and 7 Å in (f)].

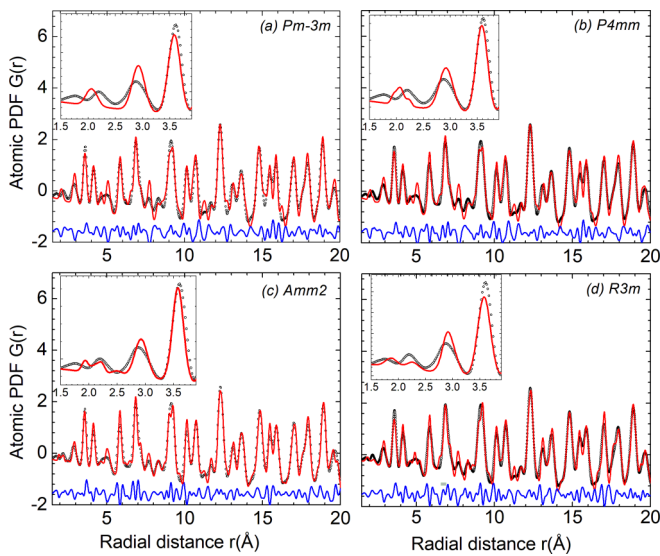


FIG. 7. (a)–(d) Experimental (symbols) and model fit (red line) atomic pair distribution functions (PDFs) for $\text{BaTi}_{0.7}\text{Ce}_{0.3}\text{O}_3$. The models are constrained to crystalline lattices where Ti and Ce atoms occupy identical oxygen octahedra. The type of the lattice is shown for each of the fits. Notably, the octahedra are not distorted for the cubic model and distorted for the other models, leading to the appearance of different ME -oxygen bonding distances. The low- r part of the PDFs is shown in the insets. For clarity, the residual difference (blue line) is shifted by subtracting a constant. The rhombohedral (space group $R3m$) model reproduces the presence of two nearest neighbor ME -O distances [$\sim 1.77(1)$ and $2.20(1)$ Å] in the experimental data better in comparison with the other models. However, the model does not reproduce well the relatively increased number of longer ME -oxygen distances in comparison with that of the shorter ones, as the misfit in the region of r values from ~ 2.0 to 2.30 Å shows. As discussed in the text, that increase is because the majority Ti-O_6 octahedra are and minority Ce-O_6 octahedra are not rhombohedrally distorted in $\text{BaTi}_{1-x}\text{Ce}_x\text{O}_3$ solid solutions for $0 \leq x \leq 0.3$. This leads to Ce-O bonds contributing to the PDF peaks at about $2.20(1)$ Å alone, thus rendering its intensity increase faster with x in comparison with that of the PDF peak at about $1.77(1)$ Å.

Considering that the Ce-oxygen bonding distance in undistorted Ce-O octahedra is about $2.24(1)$ Å, we explored a more complex model fit featuring a superposition of properly weighted PDFs for rhombohedral BaTiO_3 , where Ti-O octahedra are distorted, and room temperature orthorhombic BaCeO_3 , where Ce-O octahedra are not distorted. Fit results are shown in Fig. 6(e). The model reproduced both the shorter and longer ME -oxygen bonding distances in $\text{BaTi}_{0.7}\text{Ce}_{0.3}\text{O}_3$, including the increased relative number of the latter in comparison with that of the former, as reflected by the different intensity of the respective PDF peaks. The result indicates that the solid solutions are likely to accommodate both rhombohedrally distorted Ti-oxygen octahedra exhibiting three short and three long Ti-oxygen bonds, and nondistorted Ce-oxygen octahedra exhibiting a unique Ce-oxygen bond, whose length is close to that of the longer Ti-O bonds. The result does not imply that $\text{BaTi}_{1-x}\text{Ce}_x\text{O}_3$ ferroelectrics appear as a mixture of BaTiO_3 and BaCeO_3 phases because this model does not reproduce the higher- r features of the experiment PDF data to

an acceptable level [e.g., see the PDF peaks at 5 and 7 Å in Fig. 6(f)].

Structure models for perovskites incorporating distinct ME -oxygen octahedra are difficult to explore based on usual crystallographic unit cells of the type considered above. Therefore, to reveal both the local and average crystal structure of $\text{BaTi}_{1-x}\text{Ce}_x\text{O}_3$ ferroelectrics in full detail, large-scale 3D models were constructed and refined against the respective PDFs using reverse Monte Carlo (RMC) computations [60]. Each of the models featured a $100 \times 100 \times 100$ Å configuration of about 80 000 Ba, Ti/Ce and oxygen atoms in due proportions cut out from a perovskite lattice, where the volume of the unit cell increased uniformly with Ce content following the trend shown in Fig. 4(a). The large size of the atomic configurations allowed us to account for the different local and average crystal structure of modeled ferroelectrics in a consistent manner, that is, to explore atomic configurations of corner-sharing ME -oxygen octahedra where each of the ME atoms can be off centered to a different degree. The configurations were refined against the total atomic PDFs using a new version of the computer program RMC++ [61]. During the refinement, restraints for bonding distances and coordination numbers in the model configurations were imposed. Here, Ti, Ce, Ba, and oxygen atoms were restrained not to approach each other closer than the sum of the respective ionic radii. Also, Ti-oxygen and Ce-oxygen first coordination numbers were restrained to stay close to six, thus accounting for the specifics of the perovskite structure. As can be seen in Fig. 8, the RMC refined models reproduce the respective experimental PDF data in very good detail. The refined model configurations are shown in Fig. 9.

IV. DISCUSSION

As refined against experimental PDFs by RMC, the large-sized structure models for $\text{BaTi}_{1-x}\text{Ce}_x\text{O}_3$ ferroelectrics provide a statistical description of their structure. Typically, such models are analyzed in terms of structural characteristics relevant to the purpose of the study. Here, we analyzed the models in terms of distribution of ME -oxygen bond angles, which as shown in Fig. 5, are very sensitive to the displacement of ME atoms from the geometrical center of the oxygen octahedra forming the underlying perovskite lattice. It is that displacement and its evolution that are indeed behind the observed nonlinear piezoelectric response of $\text{BaTi}_{1-x}\text{Ce}_x\text{O}_3$ ferroelectrics with x . Due to the specific Ti off centering, intra-octahedral oxygen-Ti-oxygen bond angles in rhombohedral BaTiO_3 show characteristic values of 85° , 89° , and 95° . On the other hand, Ti-oxygen-Ti angles are close to 180° , reflecting the fact that Ti- O_6 octahedra are not tilted with respect to each other. By contrast, Ce- O_6 octahedra in BaCeO_3 are tilted and Ce-oxygen-Ce bond angles approach 160° . The near lack of Ce off centering renders intra-octahedral oxygen-Ce-oxygen angles close to 90° . Distribution of bond angles in $\text{BaTi}_{1-x}\text{Ce}_x\text{O}_3$ ferroelectrics, as extracted from the respective 3D models, is shown in Fig. 10.

As can be seen in the figure, and as it may be expected, oxygen-Ti-oxygen bond angles in BaTiO_3 appear grouped around the aforementioned three values characteristic of rhombohedrally distorted Ti- O_6 octahedra. Due to

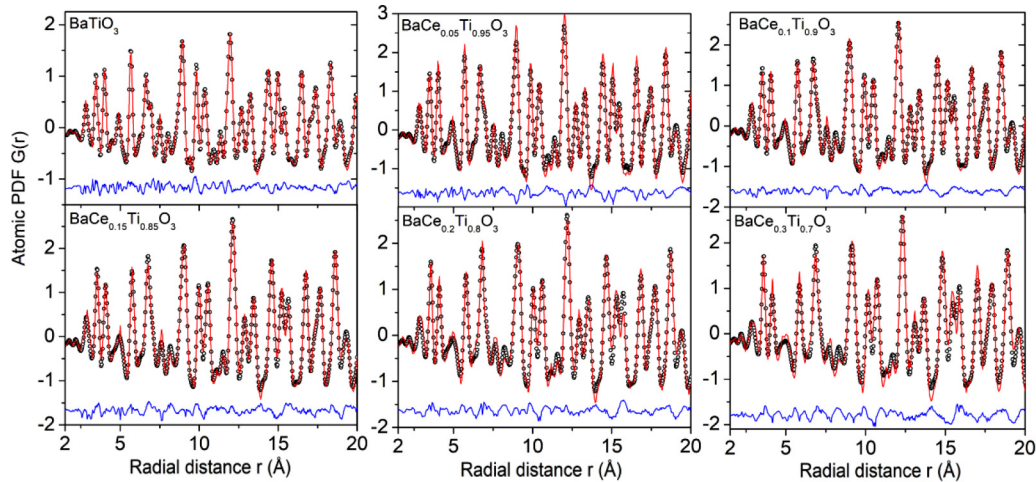


FIG. 8. Experimental (symbols) and reverse Monte Carlo (RMC) fit (red line) atomic pair distribution functions (PDFs) for $\text{BaTi}_{1-x}\text{Ce}_x\text{O}_3$ ferroelectrics. For clarity, the residual difference (blue line) is shifted by subtracting a constant. The level of agreement between the experimental and computed data is of the order of 12%, i.e., very good.

positional atomic disorder and likely deviation of Ti displacement from the $\langle 111 \rangle_c$ direction at room temperature, however, the characteristic triplet of oxygen-Ti-oxygen bonding angles in BaTiO_3 is not well resolved. For concentration of Ce < 15%, the triplet appears well resolved, indicating an increased rhombohedral distortion of Ti-O octahedra. The observation is consistent with the shift of the position of short Ti-O distances from 1.85(1) Å in BaTiO_3 to 1.80(1) Å in $\text{BaTi}_{0.85}\text{Ce}_{0.15}$ (see Fig. 3). Upon further replacement of Ce for Ti, the rhombohedral distortion increases further, and short Ti-O bonds appear at 1.77(1) Å in $\text{BaTi}_{0.7}\text{Ce}_{0.3}$. Such short Ti-O bonding distances are observed with PbTiO_3 [62,63]. Notably, the distribution of oxygen-Ti-oxygen bond angles in

$\text{BaTi}_{0.7}\text{Ce}_{0.3}$ appears somewhat smeared in comparison with $\text{BaTi}_{1-x}\text{Ce}_x\text{O}_3$ solid solutions with $x < 0.3$, resembling that in pure BaTiO_3 . Likely, this is due to increased local lattice strain arising from the different size of Ti-O₆ (10.7 Å³ in BaTiO_3) and Ce-O₆ (14.2 Å³ in CeTiO_3) octahedra forming the perovskite lattice. Furthermore, Ce-oxygen bonding distances in $\text{BaTi}_{0.7}\text{Ce}_{0.3}$ appear somewhat diminished down to 2.20(1) Å from the value of 2.24(1) Å in pure BaCeO_3 . Evidently, Ti-O₆ octahedra expand while Ce-O₆ octahedra shrink with Ce content in $\text{BaTi}_x\text{Ce}_{1-x}\text{O}_3$ solid solutions. A systematic shrinking of the longer (Zr-O) bonding distances with the relative percentage of smaller B-site atoms (Ti) has also been found in $\text{Ca}(\text{Ti}, \text{Zr})\text{O}_3$ and $\text{Ba}(\text{Ti}, \text{Zr})\text{O}_3$ solid solutions [64,65]. An inspection of Fig. 10 also shows that bond angles between Ti atoms from adjacent octahedra in $\text{BaTi}_{1-x}\text{Ce}_x\text{O}_3$ solid solutions, i.e., Ti-oxygen-Ti bond angles, remain close to 180° for all x , indicating that the octahedra do not tilt significantly with Ce content. Evidently, the local strain in the solutions is largely relieved by changes in the volume of constituent *ME*-O octahedra and not by bending of *ME*-oxygen-*ME* bond angles. The expansion of Ti-O₆ octahedra would give Ti⁴⁺ ions more room to displace from their geometrical center, thus increasing the rhombohedral distortion. The shrinking of Ce-O₆ octahedra would constrain Ce to their center, keeping them nonferroactive. Previous Raman studies also indicated the presence of two types of *ME*-oxygen polyhedra in $\text{BaTi}_{1-x}\text{Ce}_x\text{O}_3$ ferroelectrics [42,66].

With relevant structural characteristics at hand, we explored the structure-property relationship in $\text{BaTi}_{1-x}\text{Ce}_x\text{O}_3$ ferroelectrics in terms of evolution of the ferroelectric transition temperatures, polarization, and permittivity with x . Generally, the transition temperature between the ferroelectric phases of BaTiO_3 depends strongly on the magnitude and type of Ti⁴⁺ off centering [42,67]. The off centering of Ti⁴⁺ ions along $\langle 111 \rangle_c$ direction in pure BaTiO_3 , as computed from the respective 3D model, appears closer to 0.12 Å. As shown in Fig. 11(d), it increases near linearly with Ce content to a value of about 0.25 Å in $\text{BaTi}_{0.7}\text{Ce}_{0.3}\text{O}_3$. The observed increase in the rhombohedral distortion in $\text{BaTi}_{1-x}\text{Ce}_x\text{O}_3$ ferroelectrics in

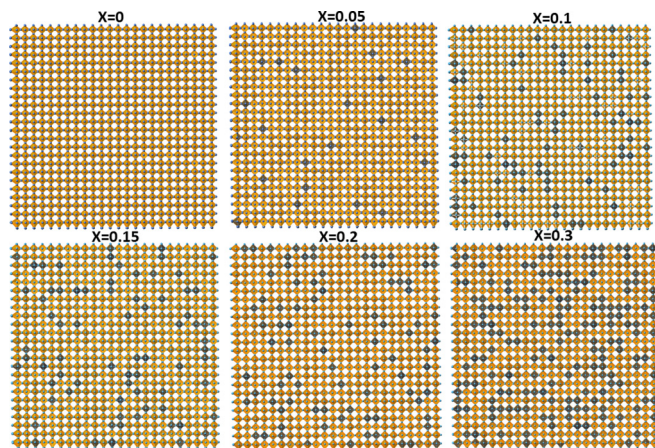


FIG. 9. Reverse Monte Carlo (RMC) refined models for $\text{BaTi}_{1-x}\text{Ce}_x\text{O}_3$ ferroelectrics featuring approximately $100 \times 100 \times 100$ Å configurations of about 80 000 Ba, Ti/Ce, and oxygen atoms in due proportions. The atoms form a perovskite lattice of corner-sharing Ti-O₆ (brown) and Ce-O₆ octahedra (dark gray). Rendition of the models highlighting areas of nearby Ce-O₆ and Ti-O₆ octahedra that exhibit nonuniform lattice strain because of the different size of the octahedra is shown in Fig. 12 introduced later.

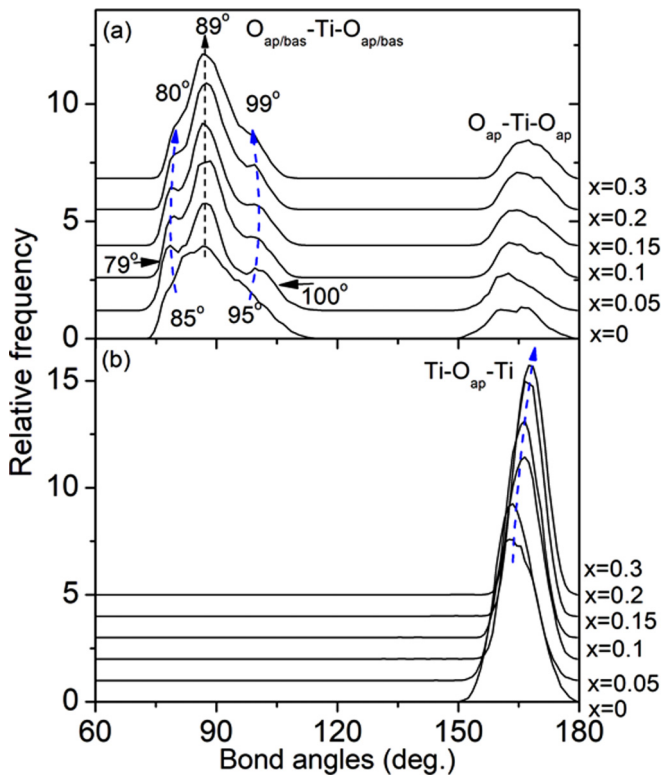


FIG. 10. Distribution of bond angles in $\text{BaTi}_{1-x}\text{Ce}_x\text{O}_3$ ferroelectrics extracted from the respective reverse Monte Carlo (RMC) refined three-dimensional (3D) models. (a) Intra-octahedral oxygen-Ti-oxygen bond angles involving at least one basal oxygen atom O_{bas} appear smeared in BaTiO_3 but clearly close to those of 85° , 89° , and 105° observed with its rhombohedral polymorph (see Fig. 5, left). The smearing is due to positional disorder of Ti atoms characteristic to room-temperature BaTiO_3 . The rhombohedral distortion intensifies in the solid solutions, as indicated by the sharpening of intra-octahedral bond angle distribution. The observation is in line with the increased difference between the shorter and longer Ti-O bonds with x (see Fig. 2). (b) The octahedra in the solid solutions do not appear tilted because Ti- O_{ap} -Ti angles involving apical oxygen atoms O_{app} tend to increase toward 180° and not to decrease toward 160° as observed with BaCeO_3 (see Fig. 5, right). Intra-octahedral bonding angles involving Ce do not change much with Ti content remaining close to 90° and therefore are not shown here.

comparison with pure BaTiO_3 would render the rhombohedral phase of the former stable to temperatures higher than the phase transition temperature T_{Rh} of 183 K observed with the latter. This would shrink the temperature range of orthorhombic and tetragonal phases with Ce content until they cease to exist, that is, the transitions between the ferroelectric phases of $\text{BaTi}_{1-x}\text{Ce}_x\text{O}_3$ would appear merged into one for a particular value of x . Indeed, this is what the experimental data for ferroelectric transition temperatures summarized in Fig. 11(c) show for low values of $x \leq 0.1$. For values of $x > 0.1$, a direct transition between the largely rhombohedral ferroelectric and cubic paraelectric phases of $\text{BaTi}_{1-x}\text{Ce}_x\text{O}_3$ may be expected to occur. However, for reasons discussed below, this transition would appear systematically shifted to lower temperature in comparison with the ferroelectric Curie temperature T_c of BaTiO_3 .

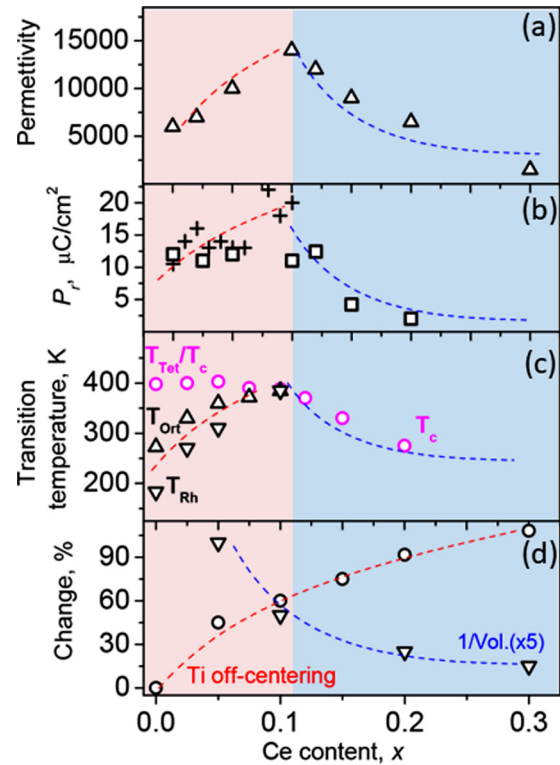


FIG. 11. Evolution of the (a) permittivity (triangles), (b) room-temperature remanent polarization P_r (squares), and (c) ferroelectric phase transition temperatures for $\text{BaTi}_{1-x}\text{Ce}_x\text{O}_3$ ferroelectrics with Ce content, x , as reported in our earlier studies [42,43]. Data for P_r (crosses) published in Ref. [69] are also shown in (b). The temperatures mark the rhombohedral-to-orthorhombic T_{Rh} (down triangles), orthorhombic-to-tetragonal T_{Ort} (up triangles), and tetragonal-to-cubic T_{Tet} (circles) phase transitions, respectively. The latter corresponds to the Curie temperature T_c , at which $\text{BaTi}_{1-x}\text{Ce}_x\text{O}_3$ solid solutions turn paraelectric. Pair distribution function (PDF) analysis derived change in Ti off centering (circles) due to a rhombohedral distortion of the perovskite lattice is shown in (d). Also shown in (d) is the reciprocal of the volume fraction occupied by Ce- O_6 and coupled to them Ti- O_6 octahedra (down triangles) in $\text{BaTi}_{1-x}\text{Ce}_x\text{O}_3$ ferroelectrics. Rendition of that volume fraction is shown in Fig. 12. Broken red lines in (a)–(d) are least squares fit to the data points for $x \leq 0.1$. The lines indicate a near linear variation of the respective data points with x . Broken blue lines in (a)–(d) represent a function of the type $1/x$. They explain well the behavior of the respective experimental datasets for $x \geq 0.1$. Altogether, data in the figure indicate the presence of two distinct regimes of the concurrent changes in the structure and ferroelectric properties of $\text{BaTi}_{1-x}\text{Ce}_x\text{O}_3$ solid solutions with the percentage of nonferroactive Ce. The regimes feature a gradual increase (red area) and accelerated decay (blue area) of the piezoelectric response for $x \leq 0.1$ and $x > 0.1$, respectively. In addition, the former involves an increase in T_{Rh} , T_{Ort} , and T_{Tet} until they merge with T_c , which stays largely unchanged. The latter involves a fast decay of T_c , i.e., cooperative ferroelectricity. Notably, though not so well expressed, the saturation polarization for $\text{BaTi}_{1-x}\text{Ce}_x\text{O}_3$ exhibits a trend like that of the remanent polarization P_r (compare data in (a) and Fig. S1 in the Supplemental Material [76]).

More specifically, the existence or absence of ferroelectricity in perovskites is determined by a balance between the short-range Coulomb-type repulsion between adjacent

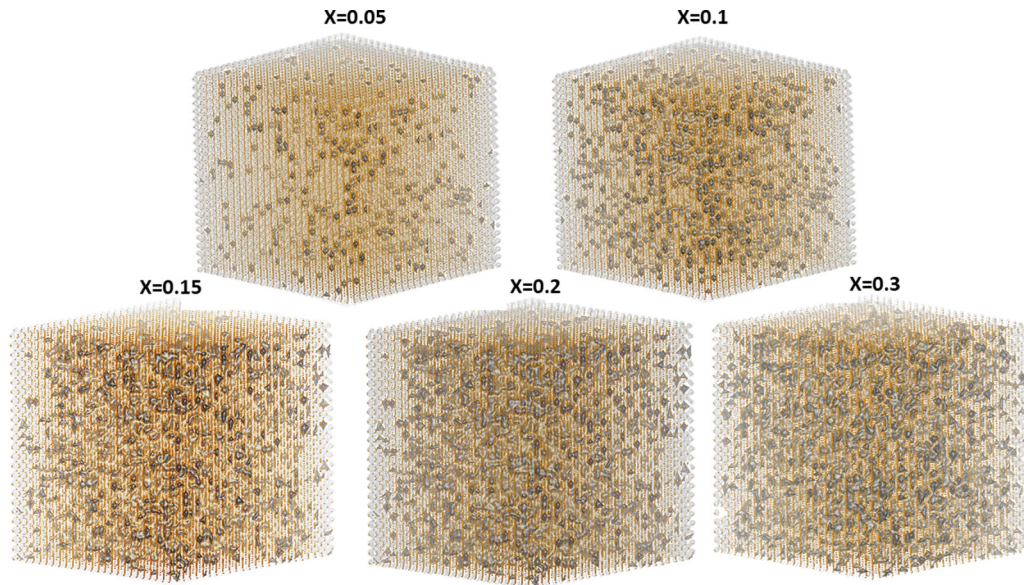


FIG. 12. Three-dimensional (3D) rendition of the perovskite lattice (brown) in the reverse Monte Carlo (RMC) refined models for $\text{BaTi}_{1-x}\text{Ce}_x\text{O}_3$ ferroelectrics shown in Fig. 9. Regions of nonuniform lattice strain arising from the presence of nearby Ti-O_6 and Ce-O_6 octahedra are shown in gray. The regions are seen to grow quickly with Ce content. Indeed, because of the accumulation of excessive lattice strain, $\text{BaTi}_{1-x}\text{Ce}_x\text{O}_3$ solid solutions are known to phase segregate for $x > 0.3$.

electron clouds and/or ions, which favors a nonferroelectric high-symmetry structure, and long-range forces due to dipole-dipole interactions, which favor a low-symmetry structure promoting ferroelectricity. The replacement of Ti^{4+} by Ce^{4+} removes electrical dipoles from the perovskite lattice in $\text{BaTi}_{1-x}\text{Ce}_x\text{O}_3$ and so would effectively weaken these forces. At a critical level of replacement of Ti^{4+} by Ce^{4+} , the long-range ferroelectric order would weaken enough for thermal excitations to overcome it, and T_c would start diminishing, reflecting the diminished long-range dipole-dipole interactions. As data in Fig. 11(c) show, this clearly occurs for values of $0.1 < x < 0.2$. At a higher concentration of Ce, the interactions would increasingly appear suppressed and, regardless of the local rhombohedral distortion of the perovskite lattice remaining large, the solutions would nearly cease to exhibit cooperative ferroelectricity. As data in Fig. 11(c) show, the latter occurs for values of $x > 0.2$. Here, it should be noted that the relatively low critical concentration of Ce ($x \sim 0.10$) at which the ferroelectricity of $\text{BaTi}_{1-x}\text{Ce}_x\text{O}_3$ perovskites starts to degrade quickly is close to the percolation threshold of the appearance of an infinite cluster of “missing dipoles” in a cubic-type lattice of dipoles where both near neighbor and next near neighbor dipole-dipole interactions are important for the emergence of a long-range order [68–73]. Evidently, removing dipoles from the perovskite lattice by substituting Ce^{4+} for Ti^{4+} ions does not simply dilute the network of dipoles but also disturbs the correlation between the direction of dipoles near Ce-O_6 octahedra and the rest of the dipoles in the lattice, leading to the observed accelerated decay of the ferroelectric properties for $x > 0.1$. A likely cause for the disturbance is the accelerated formation and growth of local strain fields in the perovskite lattice with Ce content, arising from the large size difference between corner-sharing Ce-O_6 and Ti-O_6 octahedra, as illustrated in Fig. 12. This scenario implies that, for Ce concentration $x > 0.1$, the Curie temper-

ature would vary inversely with the relative fraction of the perovskite lattice directly affected by such fields, i.e., by the volume of the lattice region occupied by interconnected Ce- and Ti-based octahedra, in $\text{BaTi}_{1-x}\text{Ce}_x\text{O}_3$. The experimental data in Figs. 11(c) and 11(d) confirm the presence of such a trend.

Concerning the remanent polarization, variations may be expected to arise from changes in the contribution of Ti^{4+} ions to the lattice polarization because both Ba^{2+} and Ce^{4+} ions are nonferroactive. An increase in the Ti^{4+} off centering with Ce content may be expected to increase the lattice and hence remanent polarization of $\text{BaTi}_{1-x}\text{Ce}_x\text{O}_3$ ferroelectrics in comparison with BaTiO_3 . Concerning the permittivity, variations may be expected to arise from changes in the polarization anisotropy. The direction of Ti off centering, i.e., direction of lattice polarization, in the not-uniformly strained clusters of corner-sharing Ti-O_6 and Ce-O_6 octahedra would appear somewhat decoupled from that in areas of the perovskite lattice free from Ce-O_6 octahedra. Effectively, this would diminish the polarization anisotropy and increase the piezoelectric response in terms of dielectric permittivity under external electric field. This scenario is consistent with the trend of the experimental data in Figs. 11(a), 11(b), and 11(d), showing a concurrent increase in Ti off centering, remanent polarization, and permittivity [42,43,66,68,69] for $x \leq 0.1$ [see Figs. 11(a) and 11(b)]. However, regardless of the further increased Ti off centering, the trend reverses for $x > 0.1$. This is because, as discussed above, the cooperative ferroelectricity in $\text{BaTi}_{1-x}\text{Ce}_x\text{O}_3$ itself starts decaying due to the critical loss of electric dipoles and growth of local strain field, leading to appearance of a broad maximum in the piezoelectric response when $x = 0.1(1)$. The concentration dependence of T_c , permittivity, and polarization of ferroelectrics from the BaTiO_3 family where Ti^{4+} is replaced by other isovalent ions, including $\text{BaTi}_{1-x}\text{Zr}_x\text{O}_3$, $\text{BaTi}_{1-x}\text{Hf}_x\text{O}_3$,

and $\text{BaTi}_{1-x}\text{Sn}_x\text{O}_3$ [27,39,40,74,75], also exhibits a nonlinear behavior of the type seen in Fig. 11, indicating the presence of a common structural origin. The difference between the rate of change in T_c , permittivity, and polarization of these ferroelectrics with the percentage of the substituent ions may be attributed to the difference in the size of those ions (0.605 Å for Ti^{4+} vs 0.69 Å for Sn^{4+} vs 0.71 Å for Hf^{4+} vs 0.72 Å for Zr^{4+} vs 0.87 Å for Ce^{4+}).

V. CONCLUSIONS

Substitution of Ce^{4+} for Ti^{4+} in BaTiO_3 modifies the atomic structure such that the ferroelectric and dielectric property changes exhibit two distinct regimes. For low Ce content, for $x \leq 0.10$, the majority Ti-O_6 octahedra in the perovskite lattice exhibit an increased rhombohedral distortion and do not have Ce-O_6 octahedra as near neighbors. Accordingly, the respective $\text{BaTi}_{1-x}\text{Ce}_x\text{O}_3$ solid solutions show an enhanced remanent polarization and increased temperature range of the rhombohedral ferroelectric phase, while the Curie temperature stays constant. Largely due to diminished polarization anisotropy, the dielectric permittivity also increases. For $x > 0.1$, the regions of nonuniform strain fields and “missing” electric dipoles arising from the increasing number of Ce atoms grow quickly, effectively diminishing both the overall lattice polarization and long-range dipole-dipole interactions. This frustrates the correlation between the directions of Ti off centering all over the perovskite lattice and, regardless of its further increased amplitude, causes an overall decay of the cooperative ferroelectricity, including a rapid decrease in the Curie temperature. Accordingly, the piezoelectric response also decays quickly in terms of both remanent polarization and permittivity. The value of $x = 0.10(\pm 2)$ appears close to the percolation threshold of the appearance of an infinite cluster of “missing dipoles” in a cubic-type lattice of dipoles where long-range correlations between the dipoles are important for the emergence of cooperative phenomena such as,

for example, ferroelectricity. Thus, because the local crystal symmetry remains rhombohedral for all x , the transition between the enhanced and diminished piezoelectric response of $\text{BaTi}_{1-x}\text{Ce}_x\text{O}_3$ ferroelectrics does not seem to involve a crossing of a morphotropic phase boundary but appears percolative in nature. To be more precise, it arises from a geometrical frustration of the ferroelectric order in a perovskite lattice that on average is pseudocubic and locally is rhombohedrally distorted for all solid solutions. In this regard, the value of $x = 0.10(\pm 2)$ appears as a tricritical point in the phase diagram of $\text{BaTi}_{1-x}\text{Ce}_x\text{O}_3$ solid solutions where the transition between the ferroelectric and paraelectric states of $\text{BaTi}_{1-x}\text{Ce}_x\text{O}_3$ changes its nature from sharp first order to continuous percolative, and the piezoelectric response is maximized. This mechanism appears to control the behavior of other ferroelectric perovskites from the BaTiO_3 family where Ti^{4+} is replaced by larger sized isovalent ions. Hence, it may need to be accounted for in the ongoing search for environmentally friendly ferroelectrics with enhanced piezoelectric response. In case the chemical substitution involves aliovalent ions, nonuniform electric fields are likely to form in addition to the strain fields. This would trigger new mechanisms affecting the ferroelectric properties. The physics of these mechanisms can also be explored using the experimental approach demonstrated here.

ACKNOWLEDGMENTS

This paper was supported by the U.S. Department of Energy, Office of Science, Office of Basic Energy Sciences under Award No. DE-SC0006877 and used resources of the Advanced Photon Source at the Argonne National Laboratory provided by the DOE Office of Science under Contract No. DE-AC02-06CH11357. Thanks are due to K. Beyer from beamline 11-ID-B for the help with synchrotron XRD experiments. Thanks are also due to K. Chapagain for the help with Rietveld analysis.

-
- [1] M. Acosta, N. Novak, V. Rojas, S. Patel, R. Vaish, J. Koruza, G. A. Rossetti, Jr., and J. Reodel, *Appl. Phys. Rev.* **4**, 041305 (2017).
 - [2] X. S. Qian, H. J. Ye, Y. T. Zhang, H. Gu, X. Li, C. A. Randall, and Q. M. Zhang, *Adv. Funct. Mater.* **24**, 1300 (2014).
 - [3] V. V. Shvartsman and D. C. Lupascu, *J. Am. Ceram. Soc.* **95**, 1 (2012).
 - [4] Y. Lin, D. Li, M. Zhang, S. Zhan, Y. Yang, H. Yang, and Q. Yuan, *ACS Appl. Mater. Interfaces* **11**, 36824 (2019).
 - [5] B. Jaffe, W. R. Cook, and H. Jaffe, *Piezoelectric Ceramics* (Academic Press, London, 1971).
 - [6] R. E. Cohen, *Nature* **358**, 136 (1992).
 - [7] G. H. Kwei, A. C. Lawson, S. J. L. Billinge, and S. Cheong, *J. Phys. Chem.* **97**, 2368 (1993).
 - [8] A. W. Hewat, *Ferroelectrics* **6**, 215 (1974).
 - [9] K. Itoh, L. Z. Zeng, E. Nakamura, and N. Mishima, *Ferroelectrics* **63**, 29 (1985).
 - [10] R. Comes, M. Lambert, and A. Guinier, *Solid State Commun.* **6**, 715 (1968).
 - [11] I. B. Bersuker, *Phys. Lett.* **20**, 589 (1966).
 - [12] A. S. Chaves, F. C. S. Baretto, R. A. Nogueira, and B. Zeks, *Phys. Rev. B* **13**, 207 (1976).
 - [13] W. Cochran, *Phys. Rev. Lett.* **3**, 412 (1959).
 - [14] W. Cochran, *Adv. Phys.* **9**, 387 (1960).
 - [15] K. A. Muller, Y. Luspain, J. L. Servoin, and F. Gervais, *J. Physique Lett.* **43**, 537 (1982).
 - [16] M. Gaudon, *Polyhedron* **88**, 6 (2015).
 - [17] K. H. Ehses, H. Bock, and K. Fischer, *Ferroelectrics* **37**, 507 (1981).
 - [18] C. Jun, F. Chan-Gao, L. Qi, and F. Duan, *J. Phys. C: Solid State Phys.* **21**, 2255 (1988).
 - [19] S. C. Abrahams, *Acta Cryst. B* **65**, 450 (2009).
 - [20] Q. Zhang, T. Cagin, and W. A. Goddard III, *Proc. Natl. Acad. Sci. USA* **103**, 14695 (2006).
 - [21] E. Stern, *Phys. Rev. Lett.* **93**, 037601 (2004).
 - [22] Y. Qi, S. Liu, I. Grinberg, and A. M. Rappe, *Phys. Rev. B* **94**, 134308 (2016).
 - [23] R. Zhang, J. Fang, and D. Viehland, *J. Am. Ceram. Soc.* **87**, 864 (2004).

- [24] Q. Sun, Q. Gu, K. Zhu, R. Jin, J. Liu, J. Wang, and J. Qiu, *Sci. Rep.* **7**, 42274 (2017).
- [25] R. Fahri, M. El. Marssi, A. Simon, and J. Ravez, *Eur. Phys. J. B* **18**, 605 (2000).
- [26] S. Lee and C. A. Randall, *Sol. State. Ion.* **249-250**, 86 (2013).
- [27] V. Buscaglia, S. Tripathi, V. Petkov, M. Dapiaggi, M. Deluca, A. Gajovic, and Y. Ren, *J. Phys.: Condens. Matter* **26**, 065901 (2014).
- [28] S. W. Kim, H. I. Choi, M. H. Lee, J. S. Park, D. J. Kim, D. Do, M. H. Kim, T. K. Song, and W. Kim, *Ceram. Inter.* **39**, S487 (2013).
- [29] Y. Liu, R. L. Withers, and B. Nguyen, *Appl. Phys. Lett.* **91**, 152907 (2007).
- [30] A. Pramanick, W. Dmowski, T. Egami, A. S. Budisuharto, F. Weyland, N. Novak, A. D. Christianson, J. M. Borreguero, D. L. Abernathy, and M. R. V. Jørgensen, *Phys. Rev. Lett.* **120**, 207603 (2018).
- [31] J. Gao, D. Xue, W. Liu, C. Zhou, and X. Ren, *Actuators* **6**, 24 (2017).
- [32] C. Ma, H. Guo, S. P. Beckman, and X. Tan, *Phys. Rev. Lett.* **109**, 107602 (2012).
- [33] T. T. A. Lummen, Y. Gu, J. Wang, S. Lei, F. Xue, A. Kumar, A. T. Barnes, E. Barnes, S. Denev, A. Belianinov, M. Holt, A. N. Morozovska, S. V. Kalinin, and L.-Q. Chen and V. Gopal, *Nat. Commun* **5**, 3172 (2014).
- [34] L. Kong, G. Liu, W. Yang, and W. Cao, *Appl. Phys. Lett.* **107**, 042901 (2015).
- [35] J. Zhuang, A. A. Bokov, N. Zhang, D. Walker, S. Huo, J. Zhang, W. Ren, and Z.-G. Ye, *Phys. Rev. B* **98**, 174104 (2018).
- [36] Q. Hu and X. Wei, *J. Adv. Dielectrics* **09**, 1930002 (2019).
- [37] S. Pal, A. B. Swain, N. V. Sarath, and P. Murugavel, *J. Phys.: Condens. Matter* **32**, 365401 (2020).
- [38] W. Liu and X. Ren, *Phys. Rev. Lett.* **103**, 257602 (2009).
- [39] J. Gao, Y. Wang, Y. Liu, X. Hu, X. Ke, L. Zhong, Y. He, and X. Ren, *Sci. Rep.* **7**, 40916 (2016).
- [40] J. Gao, Y. Liu, Y. Wang, X. Hu, W. Yan, X. Ke, L. Zhong, Y. He, and X. Ren, *J. Phys. Chem. C* **121**, 13106 (2017).
- [41] L. He, Y. Wang, J. Gao, J. Wang, T. Zhao, Z. He, Z. Zhong, X. Zhang, and L. Zhong, *Materials* **12**, 611 (2019).
- [42] G. Canu, G. Confalonieri, M. Deluca, L. Curecheriu, M. T. Buscaglia, M. Asandulesa, N. Horchidan, M. Dapiaggi, L. Mitoseriu, and V. Buscaglia, *Acta Mater.* **152**, 258 (2018).
- [43] G. Confalonieri, V. Buscaglia, G. Capitani, G. Canu, N. Rotiroti, A. Bernasconi, A. Pavese, and M. Dapiaggia, *J. Appl. Cryst.* **51**, 1283 (2018).
- [44] B. H. Toby and R. B. Von Dreele, *J. App. Cryst.* **46**, 544 (2013).
- [45] H. P. Klug and L. E. Alexander, in *X-ray diffraction procedures for polycrystalline and amorphous materials* (Wiley, New York/Sydney/Toronto, 1974).
- [46] V. Petkov, *J. Appl. Cryst.* **22**, 387 (1989).
- [47] D.-Y. Lu, D.-D. Han, X.-Y. Z. Sun, X.-L. Zhuang, and Y.-F. Zhang, *Jap. J. Appl. Phys.* **52**, 111501 (2013).
- [48] V. Krayzman and I. Levin, *J. Appl. Cryst.* **45**, 106 (2012).
- [49] S. Y. Chong, R. J. Szczecinski, C. A. Bridges, M. G. Tucker, J. B. Claridge, and M. J. Rosseinsky, *J. Am. Chem. Soc.* **134**, 5836 (2012).
- [50] N. Zhang, H. Yokota, A. M. Glazer, Z. Ren, D. A. Keen, D. S. Keeble, P. A. Thomas, and Z.-G. Ye, *Nat. Commun.* **5**, 5231 (2014).
- [51] K. Datta, R. B. Neder, J. Chen, J. C. Neufeind, and B. Mihailova, *Sci. Rep.* **7**, 471 (2017).
- [52] V. Petkov, J.-W. Kim, S. Shastri, S. Gupta, and S. Priya, *Phys. Rev. Mater.* **4**, 014405 (2020).
- [53] R. S. Roth, *J. Res. Nat. Bureau of Standards* **58**, 75 (1957).
- [54] R. Ubic, *J. Am. Cer. Soc.* **90**, 3326 (2007).
- [55] I. Levin, W. J. Laws, D. Wang, and I. M. Reaney, *Appl. Pjphys. Lett.* **111**, 212902 (2017).
- [56] K. S. Knight, *Sol. State Ionics* **74**, 109 (1994).
- [57] A. J. Jacobson, B. C. Tofield, and B. E. F. Fender, *Acta Cryst.* **28**, 956 (1972).
- [58] F. Genet, S. Loridant, C. Ritter, and G. Lucazeau *J. Phys. Chem. Sol.* **60**, 2009 (1999).
- [59] Crystallography Open Database. <http://www.crystallography.net/cod/2106994.html>.
- [60] R. L. McGreevy and L. Pusztai, *Mol. Simul.* **1**, 359 (1988).
- [61] O. Gereben and V. Petkov, *J. Phys.: Condens. Matter* **25**, 454211 (2013).
- [62] Y.-H. Shin, J.-Y. Son, B.-J. Lee, I. Grinberg, and A. M. Rappe, *J. Phys.: Condens. Matter* **20**, 015224 (2008).
- [63] T. Yamanaka, Y. Nakamoto, M. Ahart, and H.-K. Mao, *Phys. Rev. B* **97**, 144109 (2018).
- [64] I. Levin, E. Cockayne, M. W. Lufaso, and J. E. Maslar, *Chem. Mat.* **18**, 854 (2006).
- [65] I. Levin, E. Cockayne, V. Krayzman, J. C. Woicik, S. Lee, and C. A. Randal *Phys. Rev. B* **83**, 094122 (2011).
- [66] L. P. Curesheriu, M. Deluca, Z. V. Mocanu, M. V. Pop, V. Nica, N. Horchidan, M. T. Buscaglia, V. Buscaglia, M. van Bael, A. Hardy, and L. Mitoseriu, *Phase. Trans.* **86**, 703 (2013).
- [67] S. C. Abrahams, S. K. Kurtz, and P. B. Jamieson, *Phys. Rev.* **172**, 551 (1968).
- [68] C. Ang, Z. Yu, Z. Jing, R. Guo, A. S. Bhalla, and L. E. Cross, *Appl. Phys. Lett.* **80**, 3424 (2002).
- [69] K. Brajesh, A. K. Kalani, and R. Ranjan, *Appl. Phys. Lett.* **106**, 012907 (2015).
- [70] M. F. Sykes, D. S. Gaunt, and J. W. Essam, *J. Phys. A: Math. Gen.* **9**, L43 (1976).
- [71] C. D. Lorenz, R. May, and R. M. Ziff, *J. Stat. Phys.* **98**, 961 (2000).
- [72] X. Xun and R. M. Ziff, *Phys. Rev. E.* **102**, 012102 (2020).
- [73] L. Kurzawski and K. Malarz, *Rep. Math. Phys.* **70**, 163 (2012).
- [74] J. Li, D. Zhang, S. Qin, T. Li, M. Wu, D. Wang, Y. Bai, and X. Lou, *Acta Mater.* **115**, 58 (2016).
- [75] T. Shi, L. Xie, L. Gu, and J. Zhu, *Sci. Rep.* **5**, 8606 (2015).
- [76] See Supplemental Material at <http://link.aps.org/supplemental/10.1103/PhysRevMaterials.5.044410> for data for the saturation polarization of BaTi_{1-x}Ce_xO₃ BaTi1-xCexO3 solid solutions.